

Hydrodynamic Simulations of Galaxy Clusters: Scaling Relations and Evolution

N. Truong¹, E. Rasia^{2,3}, P. Mazzotta^{1,4}, S. Planelles^{5,6}, V. Biffi^{3,5}, D. Fabjan^{3,7},
A. M. Beck⁸, S. Borgani^{3,5,9}, K. Dolag⁸, G. L. Granato³, G. Murante³,
C. Ragone-Figueroa^{3,10}, L. K. Steinborn⁸

¹ Dipartimento di Fisica, Università di Roma Tor Vergata, via della Ricerca Scientifica, I-00133, Roma, Italy

² Department of Physics, University of Michigan, 450 Church St., Ann Arbor, MI 48109

³ INAF, Osservatorio Astronomico di Trieste, via Tiepolo 11, I-34131, Trieste, Italy

⁴ Harvard-Smithsonian Center for Astrophysics, 60 Gardner Street, Cambridge, MA 02138, USA

⁵ Dipartimento di Fisica dell' Università di Trieste, Sezione di Astronomia, via Tiepolo 11, I-34131 Trieste, Italy

⁶ Departamento de Astronomía y Astrofísica, Universidad de Valencia, c/Dr. Moliner, 50, 46100 Burjassot, Valencia, Spain

⁷ Faculty of Mathematics and Physics, University of Ljubljana, Jadranska 19, 1000 Ljubljana, Slovenia

⁸ University Observatory Munich, LMU, Scheinerstr. 1, D-81679, Munich, Germany

⁹ INFN, Istituto Nazionale di Fisica Nucleare, Trieste, Italy

¹⁰ Instituto de Astronomía Teórica y Experimental (IATE), Consejo Nacional de Investigaciones Científicas y Técnicas de la República Argentina (CONICET), Observatorio Astronómico, Universidad Nacional de Córdoba, Laprida 854, X50000BGR, Córdoba, Argentina

16 March 2022

ABSTRACT

We analyze hydrodynamical and cosmological simulations of galaxy clusters to study scaling relations between the cluster total masses and observable quantities such as gas luminosity, gas mass, temperature, and Y_X , i.e., the product of the last two properties. Our simulations are performed with the Smoothed-Particle-Hydrodynamic GADGET-3 code and include different physical processes. The twofold aim of our study is to compare our simulated scaling relations with observations at low ($z \approx 0$) and intermediate ($z \approx 0.5$) redshifts and to explore their evolution over the redshift range $z = 0 - 2$.

The result of the comparative study shows a good agreement between our numerical models and real data. We find that AGN feedback significantly affects low-mass haloes at the highest redshifts resulting in a reduction of the slope of the mass – gas mass relation ($\sim 13\%$) and the mass – Y_X relation ($\sim 10\%$) at $z = 2$ in comparison to $z = 0$. The drop of the slope of the mass – temperature relation at $z = 2$ ($\sim 14\%$) is, instead, caused by early mergers. We investigate the impact of the slope variation on the study of the evolution of the normalization.

We conclude that the observed scaling relations should be limited to the redshift range $z = 0 - 1$ for cosmological studies because in that redshift range the slope, the scatter, and the covariance matrix of the relations do not exhibit significant evolution. The mass – Y_X relation continues to be the most suitable relation for this goal. Extending the analysis to the redshift range between 1 and 2 will be crucial to evaluate the impact generated by the AGN feedback.

Key words: galaxies: clusters: general — galaxies: clusters: intracluster medium — X-ray: galaxy: clusters — methods: numerical

1 INTRODUCTION

Clusters of galaxies are the latest gravitationally bound structures to form. They begin their collapse at around redshift $z \sim 2$ when the dark-energy component starts to be relevant (even if not dominant yet) and just after the baryonic Universe has experienced an extremely energetic phase due to the high star formation level (Madau and Dickinson 2014) and the intense AGN (Active Galactic Nuclei) activity (Aird et al. 2015). For the reason that clusters' formation

happens in such peculiar time, these massive objects are an invaluable laboratory for the study of astrophysical processes and for the derivation of cosmological parameters.

High-redshift investigations and the comparison with local observations are particularly advantageous. One of the most powerful cosmological measure is, indeed, the *evolution* of the mass function (Borgani and Guzzo 2001; Voit 2005; Vikhlinin et al. 2009; Allen et al. 2011; Borgani and Kravtsov 2011; Planelles et al. 2015). As other example, two direct probes of the AGN-activity history are

(i) the entropy profile of local and *high-z* objects (Dubois et al. 2011; Chaudhuri et al. 2012; Ettori et al. 2013; Pointecouteau et al. 2013) and (ii) the relation between the clusters X-ray luminosity and their temperature and its evolution (Hilton et al. 2012; Takey et al. 2013; Giles et al. 2015). To decode such important measurements and to extend high-redshift studies of galaxy clusters, the X-ray community is planning and working on future missions such as e-ROSITA¹ (Merloni et al. 2012) and Athena² (Nandra et al. 2013). These will be complementary to millimetric surveys, e.g. SPT-G3 (Benson et al. 2014), or optical ones, e.g. EUCLID³ (Laureijs et al. 2011) or LSST⁴ (Ivezic et al. 2008). Both X-ray missions will build copious samples of clusters and groups of galaxies at $z \sim 1$ or above to advance high- z investigations that are currently limited mostly to $z \leq 0.7$ objects with sparse data from most distant times (Reichert et al. 2011; Maughan et al. 2012; Giodini et al. 2013).

The simplest approach to measure the mass of a large sample of objects is to access to *scaling relations* between the total mass and some observable quantities that are easier to derive. In X-rays studies, the most common mass-proxies are the *gas mass*, M_{gas} , which can be extracted from the surface brightness profile, the *temperature*, T , which is solidly estimated from X-ray spectra with, at least, one thousand of counts, and their combination, $Y_X = M_g \times T$ (e.g., Maughan 2014; Mantz et al. 2016, for recent and detailed studies on X-ray scaling relations). The Y_X parameter was firstly introduced as proxy of pressure by Kravtsov et al. (2006) who proved its advantages through the analysis of hydrodynamical simulations. Since then, it has been diffusely adopted in X-ray cosmological studies. The biggest benefit of this parameter relies on the different reactions by the gas mass and temperature in non-equilibrium situations such as a powerful AGN burst activity (Fabjan et al. 2011) that can be triggered by gravitational mergers. The AGN reduces the gas mass by expelling some gas from the core and, at the same time, it heats the ICM. Due to these behaviors the Y_X parameter does not substantially depend on the dynamical state or on the central AGN activity.

One of the X-ray measurements most represented in scaling-relation studies is the *X-ray luminosity* because it can easily and immediately be obtained from shallow observations. Scaling relations involving the luminosity, in particular the $L - M$ relation, are used to determine the connection between the flux limits of a planned survey with the minimum mass that can be observed. This relation, therefore, plays a crucial role in establishing the selection function of X-ray samples (e.g. Nord et al. 2008). The history of the $L - T$ relation has been equally important because from its first determination it was clear that this relation provides information on the physics of the cluster core (e.g., Fabian et al. 1994) and the phenomena of feedback by stars or AGN (e.g., Markevitch 1998; Maughan et al. 2012).

Over the last decade, a significant number of realistic hydrodynamical simulations enabled the study of scaling relations (Borgani and Kravtsov 2011 for a review). A special attention was dedicated to the effects of feedback from stars (Nagai et al. 2007a) and AGNs (Short and Thomas 2009; Puchwein et al. 2008; Short et al. 2010; Planelles et al. 2014; Le Brun et al. 2014; Pike et al. 2014), to the evolution of the relations up to $z \sim 1$ (Battaglia et al. 2012; Fabjan

et al. 2011; Planelles et al. 2016; Le Brun et al. 2016), and to develop a theoretical framework to exploit the simultaneous analysis of multiple signals (Stanek et al. 2010; Evrard et al. 2014). This paper, based on realistic models of ICM quantities obtained through a new BH accretion model, AGN feedback and hydro scheme, extends the analysis to $z = 2$ in vision of up-coming observational results. Most importantly, this work analyzes a simulated sample that recently proved to naturally form in a cosmological context cool-core (CC) and non-cool-core (NCC) clusters (Rasia et al. 2015). The diversity of the core entropy level in the centermost regions is mostly ascribed to the dynamical history of the system and to its overall AGN activity. We expect that in our simulated clusters the balance between radiative cooling, which forms stars, and AGN feedback, which heats the gas, is realistically reached as the systems evolve in and interact with the embedded cosmological environment. Therefore, it is compelling to study the relation between the ICM properties in an epoch right after the maximum level of the AGN activity.

The paper is arranged in the following way: in Section 2 we provide a short description of the simulated sample and refer to companion papers for a more detailed explanation of the code. Section 3 presents the computation of ICM structural quantities, the mass-proxy relations, the luminosity-based relations, and fitting methods. In Section 4, we examine the validity of our simulated data by comparing to observations at low ($z \leq 0.25$) and intermediate ($0.25 \leq z \leq 0.6$) redshifts. Section 5 is dedicated to explore the theoretical evolution of scaling relations from $z = 0$ to $z = 2$. Finally, a summary of the obtained results and conclusions is given in Section 6. All the quantities for the scaling relations are evaluated at R_{500} defined as the radius of the sphere whose density is 500 times the critical density of the Universe at the considered redshift. Throughout the paper, the symbol \log indicates the *decimal* logarithm and the uncertainty at 1σ on the best-fit parameters represents the 68.4 per cent confidence maximum-probability interval.

2 SIMULATIONS

Our analysis is based on three runs of simulated clusters. These are selected from a parent DM-only cosmological volume of $1 h^{-3} \text{Gpc}^3$ (Yoshida et al. 2001; Bonafede et al. 2011) and re-simulated at higher resolution and with the inclusion of baryons.

The re-simulated Lagrangian regions are chosen around 24 massive clusters and five isolated groups and extend a radius equal to 5 times their virial radius. Their particles, identified at redshift $z = 0$, are traced back to high redshifts (Bonafede et al. 2011) and their number is increased to achieve a better spatial and mass resolution.

The resimulations are carried out with an improved version of the GADGET-3 code (Springel 2005) where we activated the full set of SPH modifications as described in Beck et al. (2016). In short, these allow the SPH method to perform better in hydrodynamical standard tests including weak and strong shocks, gas mixing, and self-gravitating clouds.

We analyze three different runs of the same cluster sample. They differ on the level of sophistication on the description of the ICM physics. The joint analysis of the three samples allow us to qualitatively conjecture whether a possible evolution seen on the scaling relations is caused by the environment and the interac-

¹ <http://www.mpe.mpg.de/eROSITA>

² <http://www.the-athena-x-ray-observatory.eu>

³ <http://www.euclid-ec.org>

⁴ <http://www.lsst.org>

tions with the large-scale structure distribution, in case of sample-independent results, or by the astrophysical phenomena affecting the ICM, in the other situation of different outcomes depending by the sample.

- NR (Non-radiative). These simulations are carried out by the exact code used in Beck et al. (2016). The main variations with respect to the standard GADGET code include: the choice of a higher-order Wendland C^4 kernel function; a time-dependent artificial viscosity scheme; a thermal diffusion term (or artificial conduction) that improves the treatment of contact discontinuities and promotes fluid mixing. The performance of this code with respect to other particle- or grid-based codes is described in Sembolini et al. (2016b) and Sembolini et al. (2016a). These works show how the cluster simulated with the improved GADGET version (G3-XArt) performs in a similar way to grid codes, AREPO, and the most modern SPH schemes.

- CSF (Cooling, Star formation and stellar Feedback). The radiative runs consider metal-dependent radiative cooling rates accordingly to Wiersma et al. (2009) where 15 different elements (H, He, C, Ca, O, N, Ne, Mg, S, Si, Fe, Na, Al, Ar, Ni) are followed; the effect of a uniform UV/X-ray background radiation (Haardt and Madau 2001); the feedback by supernovae, as originally prescribed by Springel and Hernquist (2003); the chemical model by Tornatore et al. (2007) to account for the metal enrichment (for further details see Planelles et al. 2014). The wind velocity associated to the kinetic supernovae feedback is 350 km s^{-1} .

- AGN. This last run is built on the CSF simulations with the addition of the AGN feedback, modeled following Steinborn et al. (2015) who improved the original model by Springel (2005) by introducing a detailed and phenomenologically-driven description. The thermodynamical and metal properties and the dynamical state of the main clusters of this sample are presented also in Rasia et al. (2015), Planelles et al. (2016), and Biffi et al. (2016).

The cosmological setting is a Λ CDM model with the matter density $\Omega_m = 0.24$, the dark energy density $\Omega_\Lambda = 0.76$, $n_s = 0.96$, the amplitude of the density fluctuation power spectrum $\sigma_8 = 0.8$, and the Hubble parameter $H = 72 \text{ km s}^{-1} \text{ Mpc}^{-1}$. The observational data, presented in Section 4, are rescaled to the simulated cosmology.

The Plummer gravitational softening of the DM particles is equivalent to $3.75 h^{-1} \text{ kpc}$ in physical units up to $z = 2$ and in comoving units at higher redshifts. The gas softening is, instead, fixed to the same value in comoving coordinates at all times. The mass of the DM particle is $8.47 \times 10^8 h^{-1} M_\odot$ and the initial mass of the gas particle is $1.53 \times 10^8 h^{-1} M_\odot$.

The sample includes all the objects in the high-resolution Lagrangian regions with $M_{500} > 7 \times 10^{13} E(z)^{-1} h^{-1} M_\odot$ with $E(z) = H(z)/H_0 = (\Omega_M \times (1+z)^3 + \Omega_\Lambda)^{1/2}$. The number of AGN clusters selected at any redshift of interest and the corresponding mass range are presented in Fig. 1. Notice that at the highest redshifts, $z = 1$, $z = 1.5$ and $z = 2$, our sample includes 74, 60, and 36 objects. The smallest systems at $z = 2$ contains more than 3.5×10^4 particles providing good estimates of global quantities. We do not extend the sample to smaller systems, even if we would have obtained numerically robust global measures, because none of the planned missions will reach such small masses (see Borm et al. 2014 for e-ROSITA, Pointecouteau et al. 2013 for Athena and Benson et al. 2014 for SPT-3G).

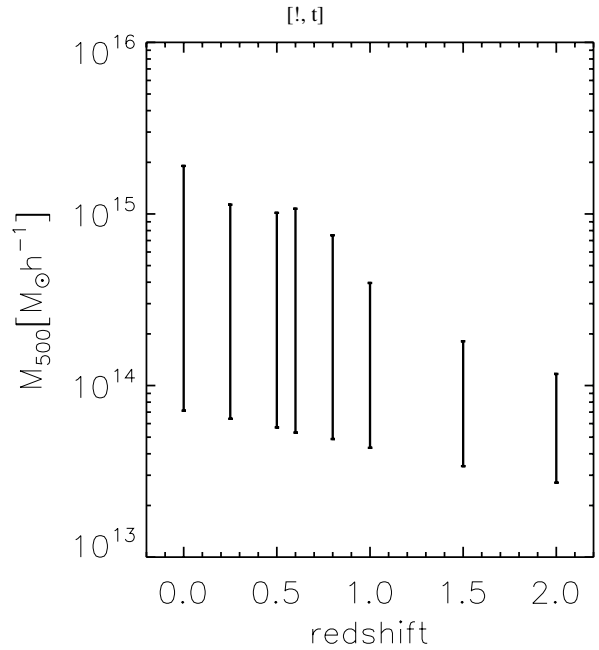


Figure 1. The vertical bars indicate the mass range considered for the AGN sample at various redshift: $z = 0, 0.25, 0.5, 0.6, 0.8, 1, 1.5,$ and 2 . The respective number of halos is 58, 75, 93, 88, 91, 74, 60, and 36.

3 METHOD OF ANALYSIS

3.1 Computing ICM Quantities

In the following, we briefly describe how we compute the relevant quantities from our simulated datasets.

Masses. The total mass, M , is calculated by summing the contribution of all the species of particles (dark-matter, gas, and stars) within R_{500} . For the gas mass, M_g , we sum up only the hot gas component⁵ of all multi-phase particles not containing more than 10% in cold mass and, therefore, no star-forming particles.

Temperatures. We consider both the mass-weighted temperature and the spectroscopic-like temperature (Mazzotta et al. 2004). The mass-weighted temperature is provided by:

$$T_{\text{mw}} = \frac{\sum_i m_i T_i}{\sum_i m_i}, \quad (1)$$

where m_i and T_i are the hot-gas mass and temperature of the i^{th} gas particle. The spectroscopic-like temperature is introduced to ease the comparison with X-ray observations and the formula was derived considering the non-flat response of the instruments on board of Chandra and XMM-Newton:

$$T_{\text{sl}} = \frac{\sum_i \rho_i m_i T_i^{0.25}}{\sum_i \rho_i m_i T_i^{-0.75}}, \quad (2)$$

where ρ_i is the particle gas density (Mazzotta et al. 2004, see also Vikhlinin 2006). For this computation, we used only particles emitting in the X-ray band with $T_i > 0.5 \text{ keV}$.

The parameter Y_X . As previously said, this parameter is equivalent to the product of gas mass and the global temperature within

⁵ The gas particles can be multi-phase, carrying information on both the hot and cold gas. The cold phase, not contributing to the gas mass, provide a reservoir for stellar formation.

R_{500} and it is a powerful proxy for the total thermal content of the ICM because it is almost insensitive to the physical processes included in simulations (Stanek et al. 2010; Fabjan et al. 2011; Battaglia et al. 2012; Sembolini et al. 2014) and to the dynamical status of the clusters (Rasia et al. 2011; Kay et al. 2012). Y_X is derived from X-ray observations, therefore we adopt the spectroscopic-like temperature in its expression:

$$Y_X = M_g \times T_{\text{sl}}. \quad (3)$$

We stress, however, that in this new set of simulations, which includes the artificial diffusion term, *the difference between the mass-weighted temperature and the spectroscopic-like one is largely reduced* (see also Biffi et al. 2016) with respect to previous results (Rasia et al. 2014). In the current $z = 0$ AGN sample, the mean and standard deviation values for the ratio $T_{\text{mw}}/T_{\text{sl}}$ computed in the sphere of radius R_{500} are equal to 1.02 and 0.10, respectively.

X-ray Luminosity. The bolometric luminosity is computed by summing up the contribution of the emissivity, ϵ_i , of all gas particles within the sphere of radius R_{500} :

$$L = \sum_i \epsilon_i = \sum_i n_{e,i} n_{H,i} \Lambda(T_i, Z_i) \Delta V_i, \quad (4)$$

where $n_{e,i}$, $n_{H,i}$ are number densities of electrons and hydrogen atoms, respectively, $\Delta V_i = m_i/\rho_i$ is the particle's volume and Λ_i is the interpolation of the cooling function pre-calculated in a fine grid of temperatures and metallicities. The cooling-function tables are created by adopting the APEC model (Smith et al. 2001) in XSPEC and by referring to the [0.01-100] keV energy band.

3.2 The Scaling Relations and the Self-Similar Prediction

The total mass of a cluster can be related to the various ICM quantities presented in the previous sections through simple power-law models. Kaiser (1986) analytically derived the functional shapes of the expected scaling relations under the assumption of virial equilibrium between the kinetic and thermal energy of a galaxy cluster and its gravitational potential (a recent extension of the formalism in dependance on the ICM physics is provided in Ettori 2015). According to this model, called self-similar (SS), the cluster total mass is the only parameter that defines both thermal and dynamical properties of the ICM (e.g., Giardini et al. 2013 and references therein).

The $M - M_g$ relation. The total mass and the gas mass are linearly related:

$$M = C_{M_g} E(z)^0 M_g, \quad (5)$$

without any dependence with the redshift. Here and in the following equations, C is a constant.

The $M - T$ relation. The total mass is related to the temperature according to:

$$M = C_T E(z)^{-1} T^{3/2}. \quad (6)$$

The $M - Y_X$ relation. From Eqs. 3, 5, and 6, the self-similar scaling of Y_X with cluster mass is given by

$$M = C_{Y_X} E(z)^{-2/5} Y_X^{3/5}. \quad (7)$$

The luminosity relations: $L - T$ and $L - M$. Assuming thermal bremsstrahlung emission, the luminosity can be related to the total mass by

$$L \propto E(z)^2 T^{1/2} f_{gas}^2 M, \quad (8)$$

[t]

Table 1. For each scaling relation (1st column): the pivot point, X_0 (2nd column), the self-similar slope, β (3rd column), and the self-similar evolution parameter, γ (4th column).

Relation	X_0	β	γ
$M - M_g$	$2 \times 10^{13} M_\odot h^{-1}$	1	0
$M - T$	3 keV	3/2	-1
$M - Y_X$	$4 \times 10^{13} M_\odot h^{-1} \text{keV}$	3/5	-2/5
$L - T_{\text{sl}}$	3 keV	2	1
$L - M$	$5 \times 10^{14} M_\odot h^{-1}$	4/3	7/3

where $f_{gas} \equiv M_g/M \equiv 1/C_{M_g}$ is the gas fraction. Given the expression of the $M - M_g$ and $M - T$ relations (Eqs. 5 and 6), the self-similar form for the $L - T$ relation is expressed as

$$L = C_{LT} E(z) T^2, \quad (9)$$

and for the $L - M$ relation as

$$L = C_{LM} E(z)^{7/3} M^{4/3}. \quad (10)$$

3.3 Fitting Method

To study the evolution of the parameters of the scaling relations, we fit them through a generic expression:

$$\log F = \log C + \gamma \log E(z) + \beta \log(X/X_0). \quad (11)$$

When F represents the total mass, M_{500} , X refers to one of the following mass-proxy: M_g , T_{mw} , T_{sl} , Y_X . Instead, when F is the X-ray luminosity, X stands for the spectroscopic-like temperature or the total mass. The value of each pivot point, X_0 is listed in Table 1. At first, we fix γ to the SS expectation values (also listed in Table 1) and we derive C and β at each *independent* redshift (Sections 5.1 and 5.2). Later, to study the evolution of the normalization, we let γ free to vary (Section 5.3).

We employ the routines provided by Kelly (2007) to investigate the parameter space and to perform the linear regression in logarithmic space. The `linmix_err.pro` routine is applied to the single linear regression with C and β as parameters. The `mlinmix_err.pro` is adopted when we include γ as free parameter. The independent variables are modeled as Gaussian distribution from which we extract the mean and standard deviation that we refer as the parameter best-fit value with its uncertainty. The Bayesian approach allows us to treat the intrinsic scatter, σ , estimated via the method of Monte Carlo Markov Chains (MCMC), as a free parameter. The MCMC is carried out by using Metropolis-Hastings (in `linmix_err.pro`) and Gibb Samplers (in `mlinmix_err.pro`) algorithms.

4 COMPARISON BETWEEN SIMULATED AND OBSERVED SCALING RELATIONS

4.1 Observational data sets

In this Section, we compare our theoretical predictions for the scaling relations with some observational results. For the mass-proxy relations, due to uncertainties associated to the amplitude of the X-ray hydrostatic mass bias derived both in observations (von der

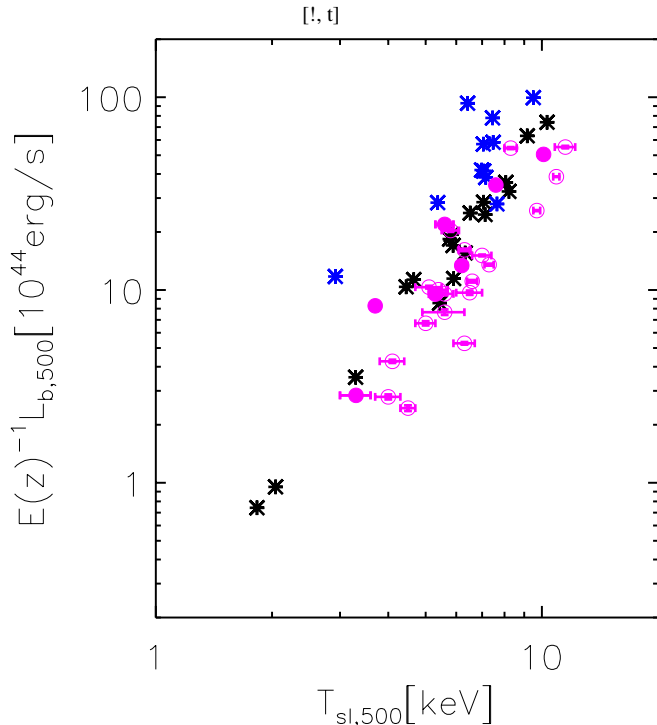


Figure 4. The $z = 0$ AGN simulated luminosity-temperature relation is shown in blue and black asterisks, respectively, for cool-core and non-cool-core systems (Rasia et al. 2015). For comparison, the cool-core and non-cool-core clusters observed by Mahdavi et al. 2013 are reported with filled and open magenta circles, respectively.

Linden et al. 2014; Maughan et al. 2015) and simulations (Nagai et al. 2007b; Rasia et al. 2012a; Biffi et al. 2016), we prefer to refer to masses estimated via the gravitational lensing technique. More specifically, we refer to Mahdavi et al. (2013), Kettula et al. (2013), and Lieu et al. (2015). The first sample contains 50 galaxy clusters in the redshift range $0.155 < z < 0.55$. The optical data are taken from the Canadian Clusters Comparison Project (CCCP, see Hoekstra et al. 2015), while the X-ray properties are based on the combined data from the *Chandra* Observatory and the *XMM-Newton* telescope. Kettula et al. (2013) analyze 10 groups with redshifts between 0.1 and 0.8 taken from the COSMOS field and observed by the Hubble Space Telescope and the XMM-Newton telescope. Lieu et al. (2015) provides X-ray observations of 38 clusters with $z < 0.6$ as part of the XXL survey. These data are associated with independent mass measurements from the Canada-France-Hawaii Telescope Lensing Survey (CFHTLenS, e.g. Heymans et al. 2012; Erben et al. 2013). The temperature measurements are restricted to the inner 300 kpc of each object.

4.2 Comparison to Observations at local and intermediate redshifts

We present the comparison between our AGN simulated scaling relations at $z = 0$ and $z = 0.5$ and those obtained from observations at $z \leq 0.25$ and at $0.25 \leq z \leq 0.6$ in Figs. 2 and 3, respectively. Each figure shows four scaling relations: $M - M_g$, $M - T_{sl}$, $M - Y_X$, and $L - M$. In this Section, all properties are measured within R_{500} without any core excision to enlighten the good match that we obtain even including the region which is the most difficult to model. For the comparison, the observational measurements of

M , M_g , Y_X and L , which depend on h^{-1} , $h^{-5/2}$, $h^{-5/2}$ and h^{-2} , have been rescaled according to the value of the Hubble parameter of the simulation. In general, we observe a satisfactory consistency between simulations and observations for all relations, especially considering that (Mahdavi et al. 2013) measurements of the masses should be increased by $\sim 20\%$ accordingly to the revised work from the group (Hoekstra et al. 2015).

The perfect accordance in the normalization of both the $M - M_g$ and $L - M$ relations assures that the simulated baryon fraction is realistic over the mass range investigated. The overall $M - T$ relation is also consistent at both redshifts. It should be noted that the temperature in Lieu et al. (2015) (brown circles in the Figures) is measured within the aperture of 300 kpc rather than within R_{500} . To compare with them, we report in the plot the simulated $M - T_{sl,300kpc}$ with a red line. Since the temperature level of the ICM is mostly reached through the shocks generated by mergers and accretion during the formation of the cluster, the good match found in the two Figures implies that these processes are realistically reproduced in our models.

To investigate in a deeper manner the influence of the central regions, we compare the $L - T$ relation measured in the two categories of cool-core and non cool-core (Fig. 4) clusters. The two simulated classes are taken from Rasia et al. (2015) and refer to the main halos of the 29 re-simulated regions. The distinction between the two types was established on the basis of the pseudo entropy level of the objects. We find reassurance in that the simulated clusters reproduce the same behavior of real systems: at a given temperature CC objects appear more luminous than NCC systems because of the higher central gas density that boosts their X-ray luminosity. The separation between CC and NCC is clearly reflected in our AGN sample, where we also find a good reproduction of the observed $L - T$ slope. This represents a step forward with respect to earlier works. Indeed, previously, two situations emerged: either the self-regulated AGN mechanism preserved the CC structures by largely enhancing the luminosities of clusters colder than 3 keV and, therefore, failing on the $L - T$ relation (Gaspari et al. 2014; Hahn et al. 2015) or, viceversa, the $L - T$ was adequately created at the expenses of a reasonable baryon census in groups and clusters cores (Puchwein et al. 2008; Gaspari et al. 2014).

5 EVOLUTION OF ICM SCALING RELATIONS

In this Section, we explore the evolution from $z = 0$ up to $z = 2$ of the six scaling relations: $M - M_g$, $M - T_{mw}$, $M - T_{sl}$, $M - Y_X$, $L - T_{sl}$, and $L - M$. All the temperatures are obtained excising the central region ($< 0.15 R_{500}$) even if excising the core produced a minimal variation. Indeed, the temperature difference is below 1% in our AGN sample and below 2% in observational samples (Maughan et al. 2012) once we compare the temperature measured in the entire sphere within R_{500} or excising the inner core region. Nevertheless, we decide to follow the standard choice, usually made to avoid the influence of the uncertainties related to the status of the core on the evolution study.

We apply the fitting procedure described in Section 3.4 and use the fitting function expressed by Eq. 11. The pivot points are equal to the values of Table 1 and the power of evolution, γ , is here fixed to the self-similar expectations introduced in Section 3. The results, in terms of best-fitting parameters and 1σ uncertainties, are reported in Tables 2 and 3 for all relations, ICM physics treatments, and for different redshifts.

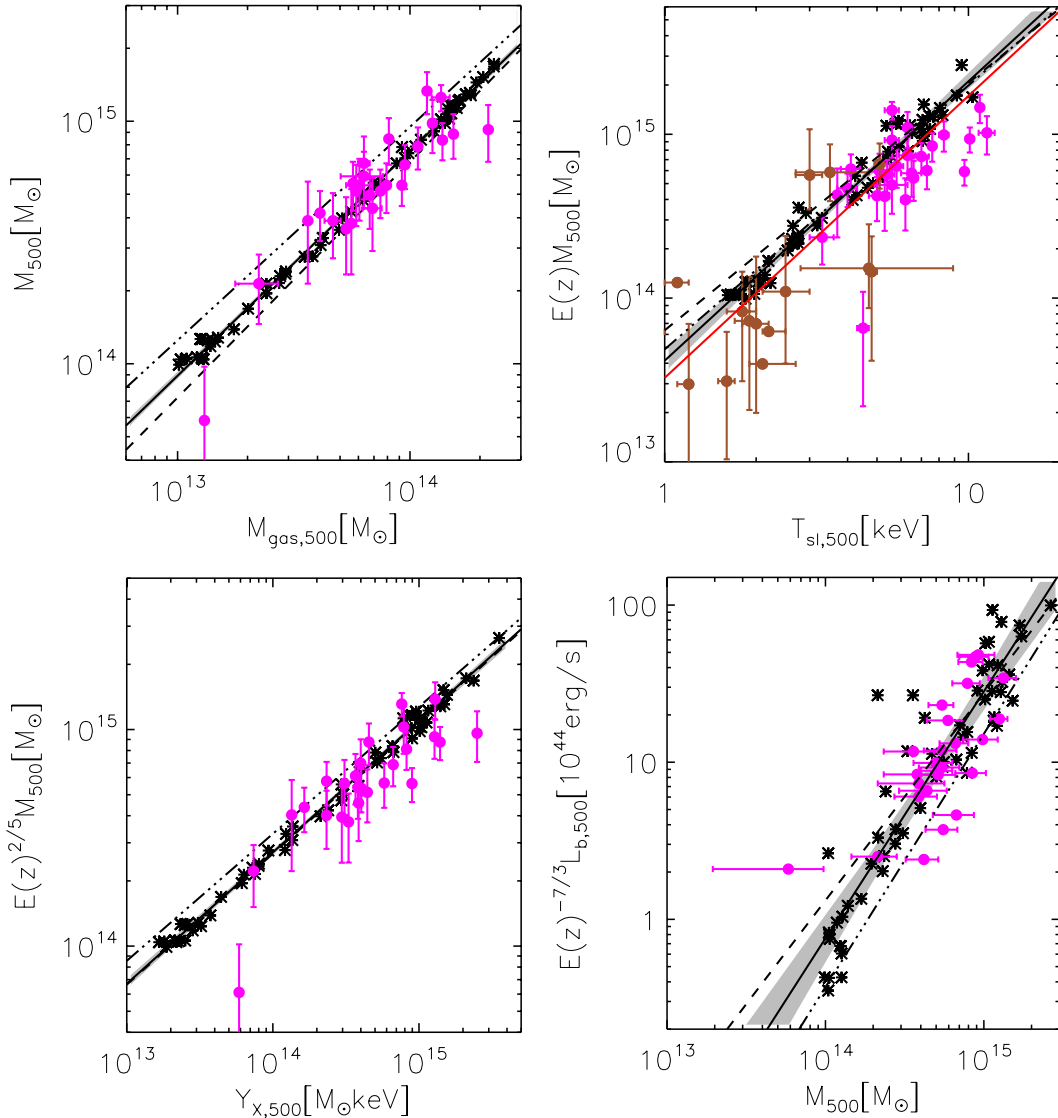


Figure 2. Comparison between simulated scaling relations at $z = 0$ and those derived from local observations ($z < 0.25$), clock-wise are the $M - M_g$, $M - T_{\text{sl}}$, $M - Y_X$, and $L - M$ relations. The observational data are taken from Mahdavi et al. 2013 (magenta), and Lieu et al. 2015 (brown) and shown with 1σ error bar. In each panel, the solid black line represents the best-fit relation of the AGN sample shown with black asterisks; the grey shaded area is the associated 1σ scatter around the best fit; the dashed and dashed-dotted lines represent the best-fit relations of the NR and CSF runs, respectively. The luminosities are bolometric, none of the quantities is core-excised, and the real data are rescaled to the cosmology adopted in the simulation.

5.1 The Slope

The evolution of the slopes of the scaling relations, β , is shown in Fig. 5 for all six scaling relations and ICM physics.

$M - M_g$ relation. The slope of the $M - M_g$ relation is approximately constant over time for the NR and CSF runs confirming the expectations: the total mass and the gas mass grow simultaneously. Indeed, dark matter and gas increase in mass by the same fraction when the mass growth happens via slow accretion (due to constant ratio between the densities of the gas and DM components in the cluster outskirts, e.g., Rasia et al. 2004) or via major merger (due to small dependence of the gas fraction on the total mass, e.g., Planelles et al. 2013; Eckert et al. 2015, and reference therein). For the same reasons, no significant evolution is measurable in the AGN runs when extending the analysis to $z \sim 1$ (in agreement with previous analysis by Fabjan et al. 2011 and Battaglia et al.

2013). However, the value of the AGN slope, β_{M_g} , decreases at $z = 1.5$ and even more at $z = 2$ to a maximum difference of $\sim 13\%$ with respect to $z = 0$. The cause of this variation relies on the scarce ability to retain the gas component by the lowest mass systems after the intense AGN activity that took place at $z > 2$. On the other hand, systems that have a total gravitational mass of $M_{500} > 5 \times 10^{13} h^{-1} M_\odot$ at this high redshift had enough gravitational potential to accelerate the accretion of the necessary gas mass that brings the $z \sim 2$ most massive objects close to the $z \sim 0$ scaling relation. In other words, at redshifts $z > 1$ the gas fraction within R_{500} evolves at different rates depending on the cluster mass. This causes the flattening of the $M - M_g$ relation at $z = 2$ with respect to $z = 0$.

Finally, we confirm previous results that compared radiative and non-radiative runs and find that the slope of the radiative runs

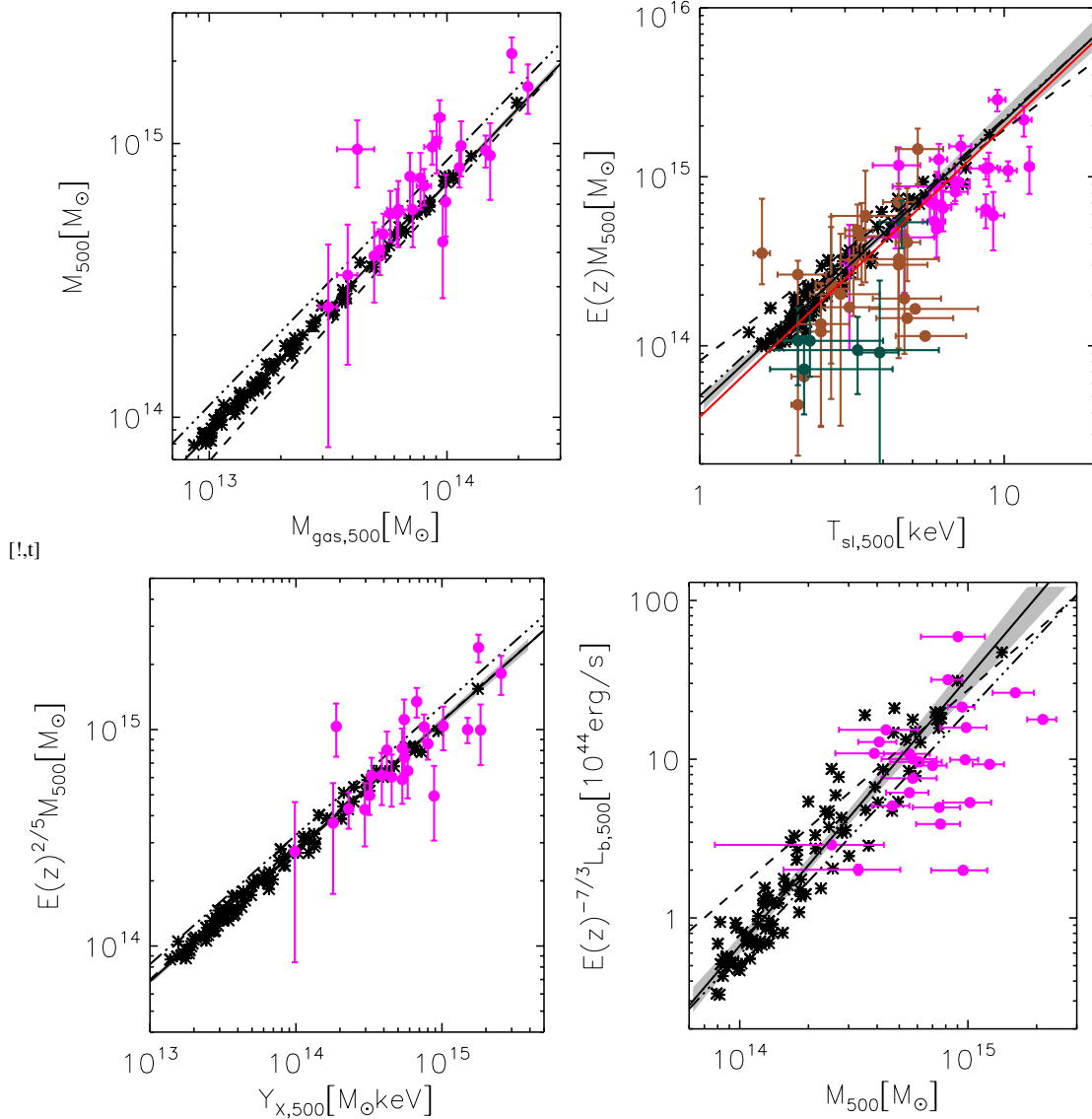


Figure 3. Comparison between simulated scaling relations at $z = 0.5$ and those derived from intermediate redshifts observations ($0.25 < z < 0.6$), clockwise are the $M - M_g$, $M - T_{sl}$, $M - Y_X$, and $L - M$ relations. Symbols and lines are similar to Figure 2. The green points and bars represent to measures and 1σ uncertainty of the groups of galaxies from Kettula et al. 2013.

is shallower (Stanek et al. 2010; Battaglia et al. 2013). This is due to the effect of radiative cooling that converts part of the hot gas into stars and that is most efficient in low massive systems. In the local universe, the AGN balance the cooling thus the slope is closer to the gravitational-only model.

$M - T_{mw}$ and $M - T_{sl}$ relations. The slopes of both temperature relations, $M - T_{mw}$ and $M - T_{sl}$, drop at high redshifts. The values $\beta_{T_{sl}}$ at $z = 2$ are reduced with respect to the $z = 0$ slope by $\sim 23\%$, $\sim 25\%$, and $\sim 14\%$ in the NR, CSF, and AGN runs, respectively. For either temperatures, the decrease in the $M - T$ slope does not strongly depend on the ICM physics. This indicates that the origin of the variation is due to macroscopic events, linked to the global evolution of the clusters.

To facilitate the explanation, we plot in Fig. 6 the $M - T_{mw}$ relation for the NR clusters at $z = 0$ and $z = 2$. As expected, high-redshift clusters are not thermalized yet and, therefore, they typically exhibit a lower value of temperature at fixed total mass,

i.e. for $E(z)M < 2 \times 10^{14} h^{-1} M_\odot$ the $z = 2$ temperatures (red points) are systematically on the left side of the $z = 0$ ones (black points). The phenomenon is present in the entire mass range but it is less pronounced for the three most massive systems at $z = 2$ that, indeed, lie extremely close to the black solid line representing the $z = 0$ scaling relation. These 3 objects have recently experienced a major merger. As consequence, their mass is doubled (notice the mass separation from the rest of the sample), and their gas has been strongly heated by the induced shocks. To secure that our result was not influenced by the limited number of objects, we verified which fraction, among the highest mass systems in the $z \sim 2.3$ MUSIC sample⁶ (Sembolini et al. 2013, 2014), has recently experienced a major merger. We found that this condition is verified for 10 systems out of the 11 objects with mass $E(z)M_{500} > 2 \times 10^{14} h^{-1} M_\odot$. We conclude that if such a massive

⁶ <http://music.ft.uam.es>

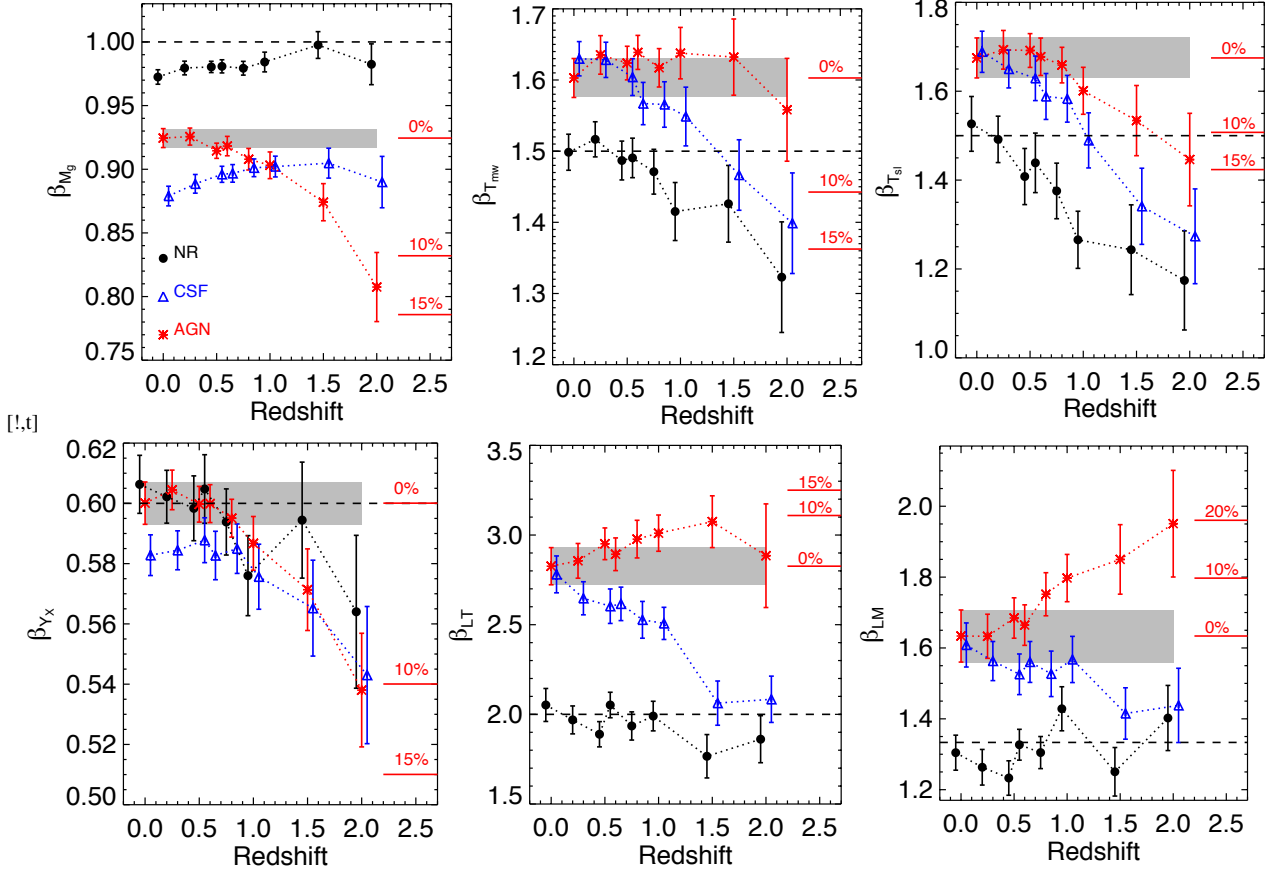


Figure 5. We show the slope value for $M - M_g$, $M - T_{mw}$, $M - T_{sl}$, $M - Y_X$, $L - T_{sl}$, and $L - M$ shown from left to right, top to bottom, respectively, as function of redshift. In each panel, the NR, CSF, and AGN runs are represented by the black circles, open blue triangles, and red asterisks. The dashed black lines represent the self-similar evolution of the slopes. The error bars represent 1σ of β parameter and the grey shaded area show this value for $z = 0$ and for the AGN sample. For this run, notice that the slopes of redshifts below 1 agree within 1σ with the $z = 0$ value, while at higher redshift they can significantly deviate. The 10%, 15% or 20% variations are reported with the red horizontal lines.

system is already present at $z = 2$ it is extremely likely (90% probability accordingly to the MUSIC sample) that it just went through a major merger phase that generated strong shocks to heat the gas. This eventuality is not surprising from a theoretical point of view since the increase steepness of the mass function at high redshift implies that it is extremely rare to grow a massive object via slow accretion. To summarize, we expect that while small clusters are not thermalized yet, the big ones can be already located in the $z = 0$ scaling relation causing a shallower slope.

The change in slope is less prominent in the AGN runs. In this circumstance, the gas of the smallest systems at $z = 2$ is warmer because of the recent and intense AGN feedback activity. The phenomenon brings the smaller objects closer to the $z = 0$ relation and reduces the amplitude of the slope evolution.

$M - Y_X$ relation. The slope of the $M - Y_X$ relation is constant until $z = 1$ and then shows a mild decrease ($\leq 10\%$) for all the ICM runs consistent with previous results by Sembolini et al. (2014) and by Pike et al. (2014). The origin of this variation can be understood by decomposing the β_{Y_X} slope into the two slopes of the $M - M_g$ and $M - T_{sl}$ (Maughan 2014):

$$\beta_{Y_X} = \frac{1}{1/\beta_{M_g} + 1/\beta_{T_{sl}}}. \quad (12)$$

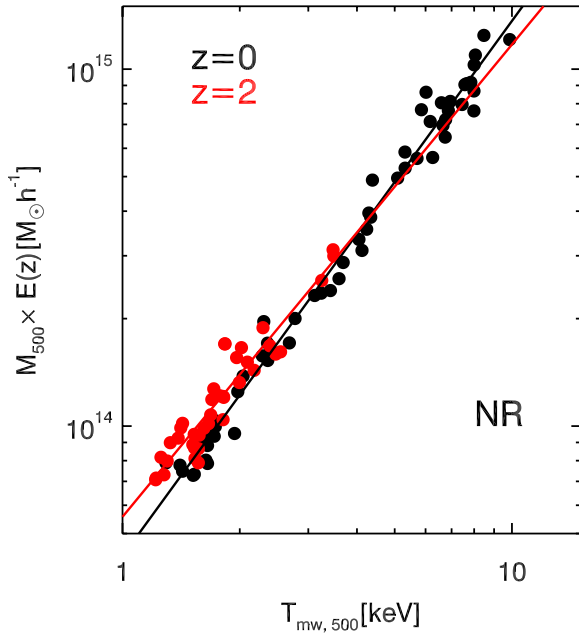
The complete derivation is presented in Appendix A. The mildness of the β_{Y_X} deviation is generated by the fact that none of the ICM

physics runs present a coincident strong variation in both β_{M_g} and $\beta_{T_{sl}}$. The NR and CSF runs have the largest variations in $\beta_{T_{sl}}$ but they have a constant β_{M_g} , viceversa, the change in β_{M_g} for the AGN run is accompanied by the mildest drop of the $\beta_{T_{sl}}$ value. From the equation is also clear why the value of the $M - Y_X$ slope is independent from the ICM prescriptions. Indeed, the AGN runs have lower β_{M_g} values than the NR simulations, because the AGN smallest systems have less gas mass at fixed total mass but they also present an higher $\beta_{T_{sl}}$ slope for the AGN extra heating that is evident in the group regime (see also discussion in Fabjan et al. 2011). This feature makes the $M - Y_X$ relation the most suitable for cosmological studies that might include clusters presenting various astrophysical properties (see also Biffi et al. 2014).

$L - T_{sl}$ and $L - M$ relations. The slopes of both luminosity-based relations are almost constant up to redshift $z = 1$. At higher redshifts, β_{LT} decreases by $\sim 10\%$ for the NR and CSF runs and β_{LM} grows by 20% in the AGN case. These changes can be again explained by the decomposition of the luminosity-based relations' slopes:

$$\beta_{LT} = \beta_{T_{sl}} \left(\frac{2}{\beta_{M_g}} - 1 \right) + \frac{1}{2}, \quad (13)$$

$$\beta_{LM} = \frac{2}{\beta_{M_g}} + \frac{1}{2\beta_{T_{sl}}} - 1. \quad (14)$$



[h]

Figure 6. Redshift evolution of the $M_{500}-T_{\text{mw}}$ scaling relation. The result is shown for the NR simulation at redshifts $z = 0$ (black) and $z = 2$ (red). The solid lines are the best fit relations corresponding to each redshift.

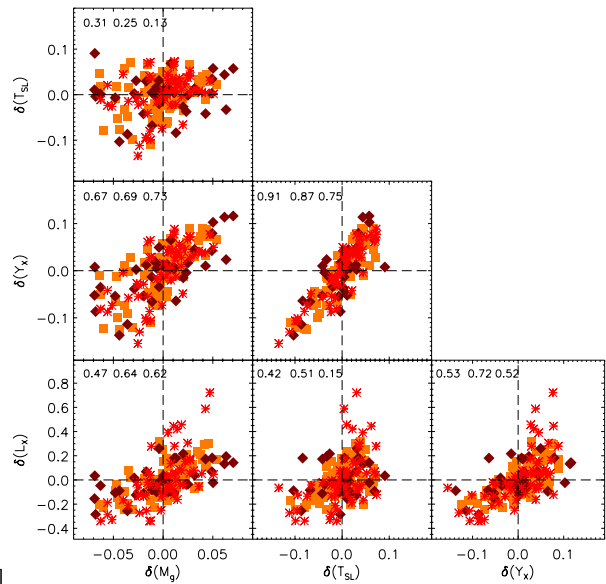
In the first case, β_{M_g} and $\beta_{T_{\text{sl}}}$ carry a similar weight leading to a counterbalance between concurrent changes. In the second case, β_{M_g} is the dominant factor, implying a variation whenever this occurs in the $M-M_g$ relation. Therefore, the steepening of the $L-M$ relation at $z > 1$ is also due to the gas depletion within the potential well of small mass systems caused by the AGN ejecta at even higher redshifts.

Another notable feature in the luminosity relations is the separation of the slope values among the three physics. The slope has a self-similar behavior for the NR simulations while β_{LT} and β_{LM} increase by 50–80% and 20–50%, respectively, in the radiative runs. The change is consistent with the previous argument on the gas fractions: radiative processes reduce the amount of gas in the simulated smallest systems and, thus, strongly lower also their total luminosity similarly to what happens in real systems. The gap between the normalization is already well established at $z = 2$ implying that at that epoch the stellar and AGN feedback in our simulated Universe already had a significant impact in establishing the energetics of clusters.

5.2 The Intrinsic Scatter

We define the scatter, σ , as the mass variance in decimal logarithm at fixed signal ($M_g, T_{\text{mw}}, T_{\text{sl}}, Y_X$) for the mass-proxy relations and as the luminosity variance in decimal logarithm at fixed T_{sl} and M_{tot} for the remaining relations. Since none of the mass-proxy scaling relations presents a significant trend with redshift, we limit the presentation in Fig. 7 to the two cases with the lowest scatter: σ_{M_g} and σ_{Y_X} . The luminosity-based relations, instead, present a variation of the scatter that decreases with redshift. We show in Fig. 7 the scatter of the $L-M$ relation. The scatter values for the remaining relations can be found in the last columns of Tables 2 and 3.

The $M-M_g$ relation always presents the minimum amount of



[h]

Figure 8. Redshift evolution of the covariance matrix between the various signals of the AGN run at three redshifts: $z = 0$ (red asterisks), $z = 1$ (orange squares), $z = 2$ (brown diamonds). The Pearson correlation coefficients for $z = 0, 1,$ and 2 are reported in each panel, respectively, from the left to the right.

scatter in line with the results from Stanek et al. (2010) and Fabjan et al. (2010). The values are around 2–3% which are 1.5 times smaller than σ_{Y_X} and a factor of 2–4 smaller than the scatter of the two temperatures ($\sigma_{T_{\text{mw}}} = 0.05$ and $\sigma_{T_{\text{sl}}} \sim 0.10$, respectively). The scatter of these four relations at $z = 2$ is always consistent within 1σ with the $z = 0$ scatter.

The two luminosity-related scaling relations $L-T$ and $L-M$ have the highest intrinsic scatter. They reach 0.2 at $z = 0$ and decrease to 0.1–0.15 at $z = 2$. The largest variation affects the $L-M$ relation. The increase of the scatter in more recent times indicates that the luminosity is sensible to the entire merging history of the clusters and that the most significant deviations from the global scaling relation are originated by recent ($z < 1$) massive mergers. A similar trend in the luminosity scatter was recently found by the Weight-the-Giant team (Mantz et al. 2016). The variation of the $L-M$ scatter with redshift is an important factor that needs to be considered for cosmological studies. Likely, the change goes in the direction of reducing the Eddington bias caused by the different scattering of objects across the threshold of a flux limited sample (e.g., Stanek et al. 2006; Maughan et al. 2012). Finally, radiative phenomena as stellar or AGN feedback have also effect onto diversifying the systems’ luminosity. Indeed, both the CSF and AGN runs show a 50% higher scatter than the NR simulations.

As second step, we investigated the shape of the deviation of each signal, δ , at fixed mass and the covariance matrix between two sets of deviations of two different signals. The scatter at fixed mass can always be accurately described by log-normal distributions (see also Le Brun et al. 2016) with a dispersion that is almost constant over time. The deviations from the scaling relations of the diverse signals are compared to each other in Fig. 8 where we report the results of the AGN sample for $z = 0, 1,$ and 2 . This analysis allows to identify which couples of signals have high correlation or anticorrelation ($|r| > 0.5$) and, therefore, can be used jointly to reduce the mass scatter with respect to the scatter of the individual scaling relations (Stanek et al. 2010).

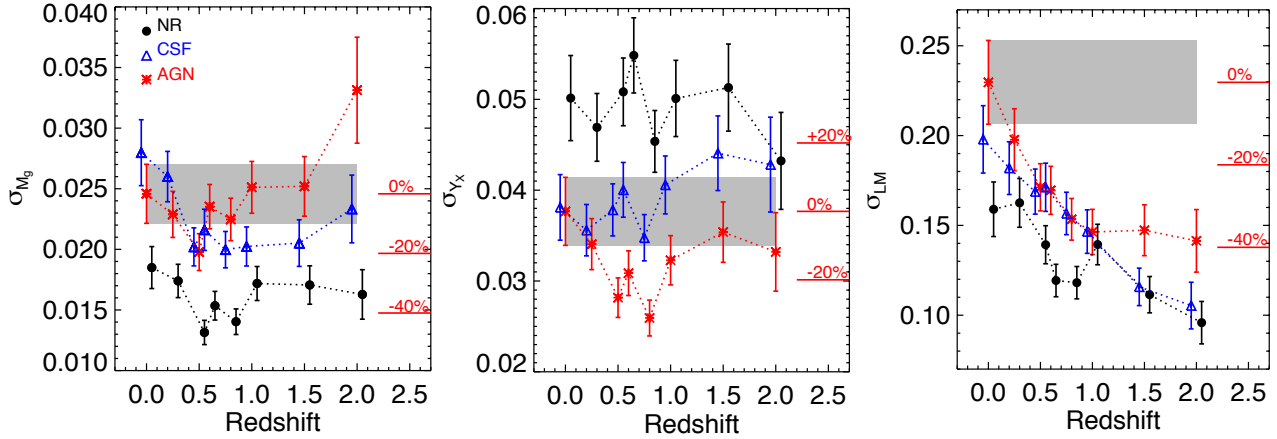


Figure 7. The evolution of intrinsic scatter for $M - M_g$ (left), $M - Y_X$ (middle), and $L - M$ (right) are shown with three simulations. The error bars present the $1 - \sigma$ limit, and the grey shaded area stands for the 68% uncertainty of the AGN intrinsic scatter at $z = 0$.

All the couples of X-ray quantities present positive correlation at all redshifts with the exception of no correlation found between δ_{M_g} and $\delta_{T_{sl}}$ and between δ_L and $\delta_{T_{sl}}$ at $z = 2$. The former behavior is consistent with the already-discussed argument about the different timescales on the variation of M_g and T_{sl} in reaction to mergers and accretion: since the two quantities increase at independent times we do not expect particular correlation. No correlation between $\delta_{T_{sl}}$ and δ_L is also expected at high redshifts. Indeed, from one side, mergers produce an increase of both luminosity and temperature generating a positive correlation between the two deviations. From the other side, strong AGN bursts, common phenomena at these redshifts, are likely to cause an increase of temperature joint by a temporary *decrease* of luminosity, due to the gas lost as ejected material. This produces a negative correlation. The correlation value that we find between δ_L and $\delta_{T_{sl}}$ at $z \leq 1$ is in good agreement with the value $r = 0.56 \pm 0.10$ found by Mantz et al. (2016) in a $z < 0.5$ sample comprehensive of both relaxed and unrelaxed clusters. In this observational paper, the authors claim a clean separation between the two classes of systems: CC relaxed systems tend to have higher δ_L and δ_T than the highly-disturbed NCC objects in their sample. In our simulations, we find that the six CC systems which are mostly X-ray regular have, indeed, the largest positive deviation on both quantities. However, we also have 5 CC systems that have negative variations in both quantities, particularly in temperature. Most of these objects have (colder) substructures that are entering in the cluster and are located in system outskirts. These increased the total mass of the object and lowered its overall ICM temperature.

The Y_X parameter shows a strong positive correlation with Pearson coefficient $r > 0.5$. Clusters deviate from the $M - Y_X$ mostly due to the changes in their temperature (Rasia et al. 2011) and this is confirmed by the fact that the highest correlation value is that between Y_X and T_{sl} .

The luminosity is also firmly correlated with the other quantities. Finally, we confirm that a combination of the luminosity and temperature ($M \propto L \times T$) as proposed in Ettori (2013) is a good approach to reduce the scatter with respect to the scatters of the individual relations $M - L$ and $M - T$.

5.3 The Normalization

The evolution of the normalization is mostly expressed as a power γ of the factor $E(z)$ (Mantz et al. 2016). In this Section, we want to enlighten how this procedure is inaccurate *whenever the slope of the considered scaling relation varies with time* (Branchesi et al. 2007). In this case, indeed, it is not possible to quantify any change in the normalization because the relation does not move in a parallel way in the scaling-relation plane.

From observations, we still do not have any indication of evolution of β for the paucity of observed $z \sim 1$ clusters. The situation will improve thanks to the collection of high- z data from SPT-3G (Benson et al. 2014) or e-Rosita (Giardini et al. 2013) and thanks also to the development of Bayesian techniques (see LIRA by Sereno and Ettori 2015a and Sereno 2016 and also Andreon and Hurn 2012). To provide forecast on the precision with which these missions will measure cosmological parameters, there are studies that perform the analysis of samples including clusters at different redshifts. The usual approach is to fix the slope either to the local β (e.g. Clerc et al. 2014) or to simultaneously fit low-, intermediate- and high-redshift objects (e.g. Hilton et al. 2012, Giles et al. 2015) letting β free to vary.

To warn about the application of these methods we focus on the $M - M_g$ and $L - M$ relations because they exhibit the largest variation in their slopes and, therefore, they are the best suited to evidence the possible mis-interpretation of the data. We build a sample that includes all the AGN simulated clusters from $z = 0$ to $z = 2$ and following the observational approach we fit this combined sample with the Eqn. (11) where the evolution factor γ , the slope β and the normalization C are all free to vary and the $E(z)$ factor is appropriately considered. With this procedure, we are therefore implying that the slope value is independent from the redshift. The best-fit parameters and their 1σ errors are reported in Table 4.

In Fig.9, we focus on 4 redshift bins ($z = 0, 0.5, 1, 1.5$, and 2) of the $M - M_g$ and $L - M$ best-fit relations of the AGN runs and we report the difference between Eq. 11 expressed through the parameters reported in Table 4 and the redshift-related factor $E(z)$ and Eq. 11 expressed with the redshift-dependent values listed in Tables 2 and 3. From the Figure, it is clear that the results obtained by enforcing the same slope can significantly deviate from the results obtained in the limited redshift bin. The most severe deviations are present at higher redshifts and for the $L - M$ relation. The $M - M_g$

[!:]

Table 2. Best-fit normalization, slope, and intrinsic scatter of the $M - M_g$, $M - T_{\text{mw}}$, $M - T_{\text{sl}}$, and $M - Y_X$ relations for the NR, CSF, and AGN runs. The parameters are obtained by a Bayesian fitting of Equation(11) with X_0 and γ give in Table 1. The uncertainties correspond to the standard deviation of the marginalized distribution for each parameter.

$M - M_g$		NR			CSF			AGN		
z	$\log C$	β	σ	$\log C$	β	σ	$\log C$	β	σ	
0.0	14.149 ± 0.003	0.972 ± 0.006	0.018 ± 0.002	14.345 ± 0.004	0.879 ± 0.008	0.028 ± 0.003	14.221 ± 0.004	0.924 ± 0.007	0.025 ± 0.002	
0.2	14.135 ± 0.002	0.980 ± 0.005	0.017 ± 0.001	14.314 ± 0.003	0.889 ± 0.007	0.026 ± 0.002	14.205 ± 0.003	0.926 ± 0.007	0.023 ± 0.002	
0.5	14.132 ± 0.001	0.980 ± 0.004	0.013 ± 0.001	14.298 ± 0.002	0.896 ± 0.006	0.020 ± 0.002	14.203 ± 0.002	0.915 ± 0.006	0.020 ± 0.002	
0.6	14.128 ± 0.002	0.981 ± 0.005	0.015 ± 0.001	14.290 ± 0.003	0.897 ± 0.007	0.022 ± 0.002	14.199 ± 0.003	0.918 ± 0.008	0.024 ± 0.002	
0.8	14.121 ± 0.002	0.979 ± 0.005	0.014 ± 0.001	14.276 ± 0.003	0.901 ± 0.007	0.020 ± 0.001	14.191 ± 0.003	0.908 ± 0.008	0.022 ± 0.002	
1.0	14.121 ± 0.002	0.984 ± 0.008	0.017 ± 0.001	14.266 ± 0.004	0.902 ± 0.008	0.020 ± 0.002	14.187 ± 0.004	0.903 ± 0.010	0.025 ± 0.002	
1.5	14.119 ± 0.004	0.998 ± 0.011	0.017 ± 0.002	14.252 ± 0.006	0.905 ± 0.012	0.021 ± 0.002	14.174 ± 0.007	0.874 ± 0.015	0.025 ± 0.002	
2.0	14.113 ± 0.008	0.982 ± 0.016	0.016 ± 0.002	14.231 ± 0.014	0.890 ± 0.020	0.023 ± 0.003	14.140 ± 0.017	0.807 ± 0.027	0.033 ± 0.004	
$M - T_{\text{mw}}$		NR			CSF			AGN		
z	$\log C$	β	σ	$\log C$	β	σ	$\log C$	β	σ	
0.0	14.351 ± 0.007	1.498 ± 0.025	0.052 ± 0.005	14.240 ± 0.007	1.630 ± 0.024	0.048 ± 0.005	14.301 ± 0.008	1.603 ± 0.027	0.052 ± 0.005	
0.2	14.354 ± 0.006	1.517 ± 0.025	0.053 ± 0.004	14.243 ± 0.006	1.628 ± 0.025	0.050 ± 0.004	14.294 ± 0.006	1.635 ± 0.027	0.053 ± 0.005	
0.5	14.379 ± 0.006	1.487 ± 0.027	0.051 ± 0.004	14.271 ± 0.005	1.604 ± 0.026	0.045 ± 0.003	14.313 ± 0.004	1.624 ± 0.024	0.043 ± 0.003	
0.6	14.387 ± 0.006	1.491 ± 0.028	0.054 ± 0.004	14.277 ± 0.006	1.567 ± 0.030	0.055 ± 0.004	14.312 ± 0.005	1.639 ± 0.024	0.041 ± 0.003	
0.8	14.373 ± 0.007	1.471 ± 0.031	0.052 ± 0.004	14.279 ± 0.006	1.566 ± 0.032	0.051 ± 0.004	14.309 ± 0.005	1.617 ± 0.027	0.041 ± 0.003	
1.0	14.381 ± 0.009	1.415 ± 0.041	0.062 ± 0.005	14.293 ± 0.007	1.549 ± 0.041	0.061 ± 0.005	14.316 ± 0.006	1.638 ± 0.036	0.049 ± 0.004	
1.5	14.405 ± 0.013	1.426 ± 0.054	0.059 ± 0.006	14.324 ± 0.010	1.466 ± 0.050	0.052 ± 0.005	14.335 ± 0.009	1.632 ± 0.054	0.047 ± 0.005	
2.0	14.377 ± 0.020	1.323 ± 0.078	0.058 ± 0.007	14.311 ± 0.014	1.399 ± 0.071	0.047 ± 0.006	14.325 ± 0.013	1.558 ± 0.072	0.043 ± 0.006	
$M - T_{\text{sl}}$		NR			CSF			AGN		
z	$\log C$	β	σ	$\log C$	β	σ	$\log C$	β	σ	
0.0	14.419 ± 0.016	1.527 ± 0.062	0.124 ± 0.012	14.234 ± 0.013	1.689 ± 0.046	0.085 ± 0.008	14.298 ± 0.013	1.675 ± 0.045	0.084 ± 0.008	
0.2	14.423 ± 0.013	1.492 ± 0.052	0.108 ± 0.009	14.261 ± 0.009	1.650 ± 0.043	0.082 ± 0.007	14.302 ± 0.009	1.693 ± 0.044	0.079 ± 0.007	
0.5	14.461 ± 0.015	1.408 ± 0.063	0.118 ± 0.009	14.296 ± 0.009	1.629 ± 0.050	0.088 ± 0.007	14.321 ± 0.007	1.692 ± 0.038	0.066 ± 0.005	
0.6	14.480 ± 0.017	1.439 ± 0.067	0.126 ± 0.010	14.306 ± 0.009	1.588 ± 0.052	0.090 ± 0.007	14.321 ± 0.008	1.678 ± 0.042	0.069 ± 0.005	
0.8	14.437 ± 0.015	1.376 ± 0.063	0.104 ± 0.008	14.294 ± 0.009	1.583 ± 0.053	0.079 ± 0.006	14.312 ± 0.007	1.659 ± 0.040	0.061 ± 0.005	
1.0	14.425 ± 0.018	1.266 ± 0.064	0.104 ± 0.008	14.303 ± 0.011	1.489 ± 0.062	0.087 ± 0.007	14.316 ± 0.009	1.601 ± 0.053	0.069 ± 0.006	
1.5	14.427 ± 0.029	1.243 ± 0.101	0.108 ± 0.010	14.337 ± 0.018	1.341 ± 0.086	0.094 ± 0.008	14.338 ± 0.014	1.534 ± 0.079	0.073 ± 0.007	
2.0	14.379 ± 0.031	1.174 ± 0.111	0.084 ± 0.010	14.307 ± 0.023	1.274 ± 0.107	0.079 ± 0.010	14.328 ± 0.021	1.446 ± 0.104	0.066 ± 0.009	
$M - Y_X$		NR			CSF			AGN		
z	$\log C$	β	σ	$\log C$	β	σ	$\log C$	β	σ	
0.0	14.143 ± 0.009	0.607 ± 0.010	0.050 ± 0.005	14.203 ± 0.006	0.583 ± 0.007	0.038 ± 0.004	14.141 ± 0.007	0.600 ± 0.007	0.038 ± 0.004	
0.2	14.142 ± 0.006	0.602 ± 0.009	0.047 ± 0.004	14.195 ± 0.004	0.584 ± 0.006	0.036 ± 0.003	14.134 ± 0.004	0.604 ± 0.007	0.034 ± 0.003	
0.5	14.163 ± 0.005	0.599 ± 0.011	0.050 ± 0.004	14.200 ± 0.004	0.588 ± 0.008	0.038 ± 0.003	14.144 ± 0.003	0.600 ± 0.006	0.028 ± 0.002	
0.6	14.167 ± 0.006	0.606 ± 0.011	0.055 ± 0.004	14.200 ± 0.004	0.583 ± 0.008	0.040 ± 0.003	14.143 ± 0.003	0.600 ± 0.006	0.031 ± 0.002	
0.8	14.152 ± 0.005	0.594 ± 0.011	0.045 ± 0.003	14.190 ± 0.004	0.585 ± 0.008	0.035 ± 0.003	14.139 ± 0.003	0.595 ± 0.006	0.026 ± 0.002	
1.0	14.153 ± 0.006	0.576 ± 0.013	0.050 ± 0.004	14.190 ± 0.005	0.575 ± 0.010	0.040 ± 0.003	14.142 ± 0.004	0.587 ± 0.009	0.032 ± 0.002	
1.5	14.160 ± 0.010	0.593 ± 0.019	0.051 ± 0.005	14.202 ± 0.009	0.565 ± 0.016	0.044 ± 0.004	14.153 ± 0.007	0.571 ± 0.014	0.035 ± 0.003	
2.0	14.133 ± 0.016	0.564 ± 0.025	0.043 ± 0.005	14.177 ± 0.017	0.542 ± 0.024	0.043 ± 0.005	14.146 ± 0.013	0.538 ± 0.019	0.033 ± 0.004	

and similarly the $M - Y_X$ are mostly deviant at $z = 2$ but do not vary substantially up to $z = 1$ as expected since their β value is mostly constant that redshift bin.

For the cases where the slope does not vary with time, such as $M - T_{\text{mw}}$ and $L - T$, the evolution in normalization is a well defined measurement and the usage of a unique fitting function is well justified. In particular, we find that the predicted slope and evolution of both relations are close to the self-similar expectations with the slight tendency of less negative evolution in the $M - T$ relation ($\gamma = -0.9$) and more positive evolution in the $L - T$ relation ($\gamma = 1.2$). In particular, the $L - T$ from our AGN sample, $E(z)^{1.28 \pm 0.12}$ and $\beta = 2.88$, is in line with recent results from Giles et al. (2015) who also reported a positive evolution $E(z)^{1.64 \pm 0.77}$ associated with the slope $\beta = 3.08 \pm 0.15$. This result is, however, in contrast with the measurements of the bolometric luminosity, $L_{\text{bol}} \sim 5-10 \times 10^{44} \text{ erg s}^{-1}$ of ISCS J1438+3414 at $z = 1.4$ and JKCS041 at $z = 2.2$ by Andreon et al. (2011), of XDCP J0044.0-2033 at $z = 1.579$ by Tozzi et al. (2015), and of

IDCS J1426.5+3508 at $z = 1.75$ by Brodwin et al. (2016). If local relations and self-similar evolution are assumed, all these objects appeared under-luminous for their measured temperature ($4.9_{-1.6}^{+3.4} \text{ keV}$, $7.3_{-2.6}^{+6.7} \text{ keV}$, $6.7_{0.9}^{+1.3} \text{ keV}$, and $7.6_{-1.9}^{+8.7} \text{ keV}$, respectively) or viceversa hotter for their luminosity. It is difficult to make a significant comparison for low statistics of objects, the large error bars, and the impossibility to evaluate any selection effect. It is, despite, interesting to notice that all these cases are *exceptionally* massive and almost twice as hot as our most massive clusters at $z \geq 1.5$.

6 SUMMARY AND DISCUSSION

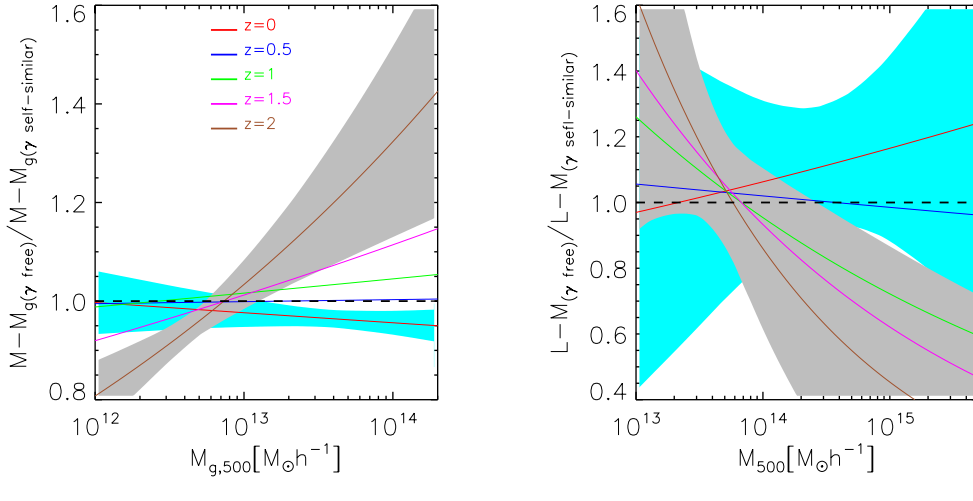
In this paper, we address the evolution of scaling relations in simulated galaxy clusters. Our study is based on a large sample of clusters, simulated in a cosmological context. The simulations are carried out with an up-graded implementation of SPH and with an improved version of the AGN physics. We first examine the reliability of our newly performed AGN runs by comparing our pre-

[!,t]

Table 3. Similar to Table 2 but for the $L - T_{\text{sl}}$ and L_M relations

$L - T_{\text{sl}}$		NR			CSF			AGN		
z	$\log C$	β	σ	$\log C$	β	σ	$\log C$	β	σ	
0.0	0.862 ± 0.024	2.045 ± 0.091	0.183 ± 0.018	0.171 ± 0.030	2.781 ± 0.103	0.196 ± 0.019	0.509 ± 0.029	2.826 ± 0.104	0.194 ± 0.019	
0.2	0.890 ± 0.019	1.967 ± 0.080	0.164 ± 0.013	0.287 ± 0.020	2.647 ± 0.092	0.182 ± 0.014	0.542 ± 0.021	2.856 ± 0.097	0.179 ± 0.015	
0.5	0.974 ± 0.017	1.887 ± 0.071	0.135 ± 0.010	0.403 ± 0.017	2.603 ± 0.096	0.164 ± 0.012	0.580 ± 0.016	2.951 ± 0.088	0.150 ± 0.011	
0.6	1.017 ± 0.018	2.054 ± 0.072	0.132 ± 0.010	0.436 ± 0.017	2.616 ± 0.093	0.157 ± 0.012	0.584 ± 0.016	2.893 ± 0.091	0.148 ± 0.012	
0.8	1.004 ± 0.018	1.935 ± 0.075	0.129 ± 0.009	0.477 ± 0.017	2.527 ± 0.103	0.155 ± 0.012	0.593 ± 0.018	2.977 ± 0.105	0.157 ± 0.012	
1.0	1.008 ± 0.022	1.989 ± 0.081	0.135 ± 0.011	0.514 ± 0.017	2.507 ± 0.090	0.133 ± 0.011	0.599 ± 0.018	3.011 ± 0.101	0.133 ± 0.011	
1.5	0.961 ± 0.031	1.768 ± 0.110	0.128 ± 0.012	0.570 ± 0.025	2.063 ± 0.123	0.135 ± 0.012	0.636 ± 0.026	3.074 ± 0.144	0.135 ± 0.013	
2.0	0.956 ± 0.037	1.865 ± 0.130	0.099 ± 0.012	0.588 ± 0.028	2.084 ± 0.129	0.091 ± 0.011	0.590 ± 0.057	2.885 ± 0.289	0.177 ± 0.022	

$L - M$		NR			CSF			AGN		
z	$\log C$	β	σ	$\log C$	β	σ	$\log C$	β	σ	
0.0	1.227 ± 0.024	1.303 ± 0.050	0.159 ± 0.015	0.925 ± 0.029	1.608 ± 0.062	0.198 ± 0.019	1.177 ± 0.034	1.634 ± 0.074	0.230 ± 0.023	
0.2	1.233 ± 0.027	1.268 ± 0.050	0.162 ± 0.013	0.985 ± 0.030	1.563 ± 0.055	0.182 ± 0.015	1.206 ± 0.034	1.633 ± 0.062	0.198 ± 0.017	
0.5	1.238 ± 0.031	1.236 ± 0.050	0.139 ± 0.011	1.035 ± 0.036	1.526 ± 0.057	0.169 ± 0.013	1.248 ± 0.035	1.685 ± 0.057	0.171 ± 0.013	
0.6	1.283 ± 0.026	1.325 ± 0.040	0.119 ± 0.009	1.071 ± 0.037	1.560 ± 0.058	0.171 ± 0.013	1.250 ± 0.037	1.665 ± 0.057	0.170 ± 0.013	
0.8	1.318 ± 0.033	1.310 ± 0.046	0.118 ± 0.009	1.120 ± 0.046	1.527 ± 0.064	0.157 ± 0.012	1.337 ± 0.044	1.752 ± 0.061	0.153 ± 0.012	
1.0	1.383 ± 0.050	1.430 ± 0.063	0.139 ± 0.011	1.169 ± 0.052	1.568 ± 0.065	0.147 ± 0.012	1.376 ± 0.051	1.797 ± 0.067	0.146 ± 0.013	
1.5	1.220 ± 0.064	1.248 ± 0.069	0.112 ± 0.010	1.084 ± 0.067	1.415 ± 0.073	0.116 ± 0.010	1.442 ± 0.089	1.850 ± 0.098	0.147 ± 0.014	
2.0	1.380 ± 0.100	1.403 ± 0.094	0.097 ± 0.012	1.150 ± 0.112	1.438 ± 0.105	0.105 ± 0.013	1.569 ± 0.159	1.951 ± 0.150	0.141 ± 0.017	



[!,t]

Figure 9. For the AGN sample we report the ratio for the $M - M_g$ (left) and $L - M$ (right) scaling relation between the expression 11 derived using the best-fit parameters from Table 4 (obtained by fitting a sample that included all the object at all redshifts) and the same expression with γ fixed at the self-similar value and the normalization and slope expressed with the parameters in Tables 2 and 3. The shaded area show the 68.3% uncertainties for two cases $z = 0$ (cyan) and $z = 2$ (grey).

[t]

Table 4. Best-fit parameters from the Bayesian fit of Equation 11 to the AGN data in the redshift range $[0 - 2]$ with γ free to vary

	$\log C$	β	γ	σ
$M - M_g$	14.208 ± 0.002	0.916 ± 0.002	-0.047 ± 0.011	0.025 ± 0.001
$M - T_{\text{mw}}$	14.297 ± 0.003	1.623 ± 0.003	-0.902 ± 0.017	0.045 ± 0.001
$M - T_{\text{sl}}$	14.297 ± 0.005	1.661 ± 0.005	-0.847 ± 0.027	0.069 ± 0.002
$M - Y_X$	14.133 ± 0.002	0.597 ± 0.002	-0.314 ± 0.013	0.032 ± 0.001
$L - T_{\text{sl}}$	0.551 ± 0.012	2.877 ± 0.012	1.161 ± 0.063	0.162 ± 0.005
$L - M$	1.228 ± 0.015	1.673 ± 0.015	2.520 ± 0.077	0.176 ± 0.005

dictions to those derived from local ($z < 0.25$) and intermediate ($0.25 < z < 0.6$) observations. Subsequently, we investigate the evolution of six scaling relations: $M - M_g$, $M - T_{\text{mw}}$, $M - T_{\text{sl}}$, $M - Y_X$, $L - T_{\text{sl}}$, and $L - M$ by comparing the AGN model with two other parallel runs performed with non-radiative physics or radiative ICM but without AGN feedback. We characterize how the scaling relation features (namely the slope, intrinsic scatter, and normalization) and the covariance matrix between couples of signals change as a function of redshift. We summarize in the following our main results.

- The simulated scaling relations at low and intermediate redshifts reproduce well the observations. Distinctly, the $L - T$ relation is well reproduced by the AGN runs that are able to reproduce its slope in a mass range from small groups to clusters and the observed separation between CC and NCC clusters.

- From $z = 0$ and $z = 1$, we do not detect any appreciable change on the slopes of the relations. At higher redshifts, however, all the relations exhibit some degree of evolution with the only exception of the luminosity-temperature slope which remains unchanged. In the AGN runs, the gas slope β_{M_g} at $z = 2$ is reduced by $\sim 13\%$ with respect to the present-time value. This is caused by the effect of intense high- z AGN activity that has more impact on the lowest mass systems. At $z = 2$, a shallower slope is found also for the $M - T$ relation that declines by $\sim 15\%$ with respect to $z = 0$. At these high redshifts, the smallest groups have a systematic low temperature due to their incomplete thermalization. The decrease of Y_X ($\sim 10\%$) and increase of $L - M$ ($\sim 20\%$) slopes can be explained by analytically decomposing their slopes in the two contributors: β_{M_g} and $\beta_{T_{\text{sl}}}$.

- We do not find any significant trend in redshift for the scatter of all the mass-proxy relations. Consistent with previous theoretical studies, the $M - M_g$ relation has the smallest scatter around 2 – 3%. Instead, the scatter of the two luminosity relations $L - T_{\text{sl}}$ and $L - M$ is the largest and around 15 – 20%, over the redshift range $[0 - 2]$. The $L - M$ scatter increases with the decrease of redshift enlightening the significant impact on the X-ray luminosity by recent major mergers (Torri et al. 2004). When a merger occurs the luminosity registers a permanent increase (Rowley et al. 2004). The scatter of all relations can be well-described by a log-normal distribution whose widths are mostly constant over the redshift up to $z \sim 1.5$.

- No correlation is evident between the pair of deviation in M_g and T_{sl} at fixed mass and at all redshift. No correlation is registered also between L and T_{sl} at $z = 2$. In all other cases, positive correlations are found with Pearson coefficients always greater than 0.4. Interestingly, the correlation coefficients are almost constant from $z = 0$ to $z = 1$ assuring that the reasons causing coupled deviations from the scaling relations are already in place at high redshift.

- Regarding the study of the evolution of the normalization, we stress that in situations where the slopes vary with redshift the evolution on the normalization cannot be established. On the other hand, we find that the $M - T_{\text{mw}}$ and $L - T_{\text{sl}}$ relations, whose slopes do not have any evolution, exhibit a negative and positive evolution of the normalization for the redshift range $[0 - 2]$, with values for the evolution parameters in line with recent observational studies and close to the self-similar predictions.

- Overall, we confirm that the $M - Y_X$ relation evaluated from $z = 0$ to $z = 1$ is the best suited for cosmological studies for the combination of its properties: in that redshift range, the slope does not vary, the evolution of the normalization can be robustly determined, the scatter is small and constant over time and most

importantly the relation is solid and independent from the source of feedback either from star, supernovae, or AGN.

On the basis of our analysis of the intrinsic variations of simulated clusters, we also conclude that pushing the study of the scaling relations at higher redshifts does not seem to be an advantage because the intense AGN activity, peaking at $z \sim 2$, could have a significant impact and produce deviations from the self-similar behavior at redshifts $z > 1$. This cosmic epoch is still almost an unexplored territory where the predictions of higher-resolution simulations can help in designing observational strategies for future missions such as e-Rosita and Athena. From an observational perspective, the scaling relations are expected to be calibrated by measuring the mass from weak-lensing analysis (Marrone et al. 2012; Hoekstra et al. 2015; Sereno and Ettori 2015a; Mantz et al. 2016). Even if this procedure is not expected to introduce mass bias (Meneghetti et al. 2010; Becker and Kravtsov 2011; Rasia et al. 2012b) it will likely enlarge the scatter of the relations (Sereno and Ettori 2015b) and attention will need to be places for clusters close to the flux limit threshold Nord et al. (2008). Certainly, more efforts will need to be devoted to reducing the uncertainties on the mass calibration to few percent level.

ACKNOWLEDGEMENTS

We are greatly indebted to Volker Springel for giving us access to the developer version of the GADGET3 code and to the entire MUSIC team to give us access to the simulated data for the comparison shown in Section 5.1. We would like to thank Gustavo Yepes, Stefano Ettori, and Mauro Sereno for providing useful discussions and comments. We acknowledge support from: PIIF-GA- 2013-627474 (E.R.); NSF AST-1210973 (E.R.); the *Spanish Ministerio de Economía y Competitividad*, MINECO, grant AYA2013-48226-C3-2-P (S.P.); the Generalitat Valenciana, grant GVACOMP2015-227 (S.P.); the *Slovenian Research Agency* (D.F.); the DFG Cluster of Excellence “Origin and Structure of the Universe” (A.M.B.); the DFG Research Unit 1254 “Magnetisation of interstellar and intergalactic medium” (A.M.B.); CONICET, FonCyT and SeCyT-UNC, Argentina (C.R.F.). This work is also supported by the PRIN-MIUR 201278X4FL “Evolution of cosmic baryons” funded by the Italian Ministry of Research, by the PRIN-INAF 2012 grant “The Universe in a Box: Multi-scale Simulations of Cosmic Structures”, by the INDARK INFN grant, by the “Consorzio per la Fisica di Trieste” Simulations were performed using Flux HCP Cluster at the University of Michigan and the Galileo Machine at CINECA with CPU time assigned through ISCRa proposals and an agreement with the University of Trieste. Data, post-processing, and storage has been done on the CINECA facility PICO, granted to us thanks to our expression of interest.

REFERENCES

- Aird J., Coil A.L., Georgakakis A., Nandra K., Barro G., Pérez-González P.G., 2015, MNRAS, 451, 1892
 Allen S.W., Evrard A.E., Mantz A.B., 2011, ARA&A, 49, 409
 Andreon S., Hurn M.A., 2012, ArXiv e-prints
 Andreon S., Trinchieri G., Pizzolato F., 2011, MNRAS, 412, 2391
 Battaglia N., Bond J.R., Pfrommer C., Sievers J.L., 2012, ApJ, 758, 74
 Battaglia N., Bond J.R., Pfrommer C., Sievers J.L., 2013, ApJ, 777, 123

- Beck A.M., et al., 2016, MNRAS, 455, 2110
- Becker M.R., Kravtsov A.V., 2011, ApJ, 740, 25
- Benson B.A., et al., 2014, in *Millimeter, Submillimeter, and Far-Infrared Detectors and Instrumentation for Astronomy VII*, vol. 9153 of *Proc. SPIE*, p. 91531P
- Biffi V., Sembolini F., De Petris M., Valdarnini R., Yepes G., Gottlöber S., 2014, MNRAS, 439, 588
- Biffi V., et al., 2016, ArXiv e-prints
- Bonafede A., Dolag K., Staszczyn F., Murante G., Borgani S., 2011, MNRAS, 418, 2234
- Borgani S., Guzzo L., 2001, Nature, 409, 39
- Borgani S., Kravtsov A., 2011, Advanced Science Letters, 4, 204
- Borm K., Reiprich T.H., Mohammed I., Lovisari L., 2014, A&A, 567, A65
- Branchesi M., Gioia I.M., Fanti C., Fanti R., 2007, A&A, 472, 739
- Brodwin M., McDonald M., Gonzalez A.H., Stanford S.A., Eisenhardt P.R., Stern D., Zeimann G.R., 2016, ApJ, 817, 122
- Chaudhuri A., Nath B.B., Majumdar S., 2012, ApJ, 759, 87
- Clerc N., et al., 2014, MNRAS, 444, 2723
- Dubois Y., Devriendt J., Teyssier R., Slyz A., 2011, MNRAS, 417, 1853
- Eckert D., et al., 2015, ArXiv e-prints
- Erben T., et al., 2013, MNRAS, 433, 2545
- Ettori S., 2013, MNRAS, 435, 1265
- Ettori S., 2015, MNRAS, 446, 2629
- Ettori S., et al., 2013, ArXiv e-prints
- Evrard A.E., Arnault P., Huterer D., Farahi A., 2014, MNRAS, 441, 3562
- Fabian A.C., Crawford C.S., Edge A.C., Mushotzky R.F., 1994, MNRAS, 267, 779
- Fabjan D., Borgani S., Tornatore L., Saro A., Murante G., Dolag K., 2010, MNRAS, 401, 1670
- Fabjan D., Borgani S., Rasia E., Bonafede A., Dolag K., Murante G., Tornatore L., 2011, MNRAS, 416, 801
- Gaspari M., Brighenti F., Temi P., Ettori S., 2014, ApJL, 783, L10
- Giles P.A., et al., 2015, ArXiv e-prints
- Godini S., Lovisari L., Pointecouteau E., Ettori S., Reiprich T.H., Hoekstra H., 2013, Space Sci. Rev., 177, 247
- Haardt F., Madau P., 2001, in D.M. Neumann, J.T.V. Tran, eds., *Clusters of Galaxies and the High Redshift Universe Observed in X-rays*, p. 64
- Hahn O., Martizzi D., Wu H.Y., Evrard A.E., Teyssier R., Wechsler R.H., 2015, ArXiv e-prints
- Heymans C., et al., 2012, MNRAS, 427, 146
- Hilton M., et al., 2012, MNRAS, 424, 2086
- Hoekstra H., Herbonnet R., Muzzin A., Babul A., Mahdavi A., Viola M., Cacciato M., 2015, MNRAS, 449, 685
- Ivezic Z., Tyson J.A., et al. for the LSST Collaboration, 2008, ArXiv e-prints
- Kaiser N., 1986, MNRAS, 222, 323
- Kay S.T., Peel M.W., Short C.J., Thomas P.A., Young O.E., Battye R.A., Liddle A.R., Pearce F.R., 2012, MNRAS, 422, 1999
- Kelly B.C., 2007, ApJ, 665, 1489
- Kettula K., et al., 2013, ApJ, 778, 74
- Kravtsov A.V., Vikhlinin A., Nagai D., 2006, ApJ, 650, 128
- Laureijs R., et al., 2011, ArXiv e-prints
- Le Brun A.M.C., McCarthy I.G., Schaye J., Ponman T.J., 2014, MNRAS, 441, 1270
- Le Brun A.M.C., McCarthy I.G., Schaye J., Ponman T.J., 2016, ArXiv e-prints
- Lieu M., et al., 2015, ArXiv e-prints
- Madau P., Dickinson M., 2014, ARA&A, 52, 415
- Mahdavi A., Hoekstra H., Babul A., Bildfell C., Jeltema T., Henry J.P., 2013, ApJ, 767, 116
- Mantz A.B., et al., 2016, ArXiv e-prints
- Markevitch M., 1998, ApJ, 504, 27
- Marrone D.P., et al., 2012, ApJ, 754, 119
- Maughan B.J., 2014, MNRAS, 437, 1171
- Maughan B.J., Giles P.A., Randall S.W., Jones C., Forman W.R., 2012, MNRAS, 421, 1583
- Maughan B.J., Giles P.A., Rines K.J., Diaferio A., Geller M.J., Van Der Pyl N., Bonamente M., 2015, ArXiv e-prints
- Mazzotta P., Rasia E., Moscardini L., Tormen G., 2004, MNRAS, 354, 10
- Meneghetti M., Rasia E., Merten J., Bellagamba F., Ettori S., Mazzotta P., Dolag K., Marri S., 2010, A&A, 514, A93
- Merloni A., et al., 2012, ArXiv e-prints
- Nagai D., Kravtsov A.V., Vikhlinin A., 2007a, ApJ, 668, 1
- Nagai D., Vikhlinin A., Kravtsov A.V., 2007b, ApJ, 655, 98
- Nandra K., et al., 2013, ArXiv e-prints
- Nord B., Stanek R., Rasia E., Evrard A.E., 2008, MNRAS, 383, L10
- Pike S.R., Kay S.T., Newton R.D.A., Thomas P.A., Jenkins A., 2014, MNRAS, 445, 1774
- Planelles S., Borgani S., Dolag K., Ettori S., Fabjan D., Murante G., Tornatore L., 2013, MNRAS, 431, 1487
- Planelles S., Borgani S., Fabjan D., Killeidar M., Murante G., Granato G.L., Ragone-Figueroa C., Dolag K., 2014, MNRAS, 438, 195
- Planelles S., Schleicher D.R.G., Bykov A.M., 2015, Space Sci. Rev., 188, 93
- Planelles S., et al., 2016, Submitted to MNRAS, 000, 000
- Pointecouteau E., et al., 2013, ArXiv e-prints
- Puchwein E., Sijacki D., Springel V., 2008, ApJL, 687, L53
- Rasia E., Tormen G., Moscardini L., 2004, MNRAS, 351, 237
- Rasia E., Mazzotta P., Evrard A., Markevitch M., Dolag K., Meneghetti M., 2011, ApJ, 729, 45
- Rasia E., et al., 2012a, New Journal of Physics, 14, 055018
- Rasia E., et al., 2012b, New Journal of Physics, 14, 055018
- Rasia E., et al., 2014, ApJ, 791, 96
- Rasia E., et al., 2015, ApJL, 813, L17
- Reichert A., Böhringer H., Fassbender R., Mühlegger M., 2011, A&A, 535, A4
- Rowley D.R., Thomas P.A., Kay S.T., 2004, MNRAS, 352, 508
- Sembolini F., Yepes G., De Petris M., Gottlöber S., Lamagna L., Comis B., 2013, MNRAS, 429, 323
- Sembolini F., De Petris M., Yepes G., Foschi E., Lamagna L., Gottlöber S., 2014, MNRAS, 440, 3520
- Sembolini F., et al., 2016a, MNRAS, 457, 4063
- Sembolini F., et al., 2016b, MNRAS, 459, 2973
- Sereno M., 2016, MNRAS, 455, 2149
- Sereno M., Ettori S., 2015a, MNRAS, 450, 3675
- Sereno M., Ettori S., 2015b, MNRAS, 450, 3633
- Short C.J., Thomas P.A., 2009, ApJ, 704, 915
- Short C.J., Thomas P.A., Young O.E., Pearce F.R., Jenkins A., Muanwong O., 2010, MNRAS, 408, 2213
- Smith R.K., Brickhouse N.S., Liedahl D.A., Raymond J.C., 2001, ApJL, 556, L91
- Springel V., 2005, MNRAS, 364, 1105
- Springel V., Hernquist L., 2003, MNRAS, 339, 289
- Stanek R., Evrard A.E., Böhringer H., Schuecker P., Nord B., 2006, ApJ, 648, 956

- Staneke R., Rasia E., Evrard A.E., Pearce F., Gazzola L., 2010, ApJ, 715, 1508
- Steinborn L.K., Dolag K., Hirschmann M., Prieto M.A., Remus R.S., 2015, MNRAS, 448, 1504
- Takey A., Schwobe A., Lamer G., 2013, A&A, 558, A75
- Tornatore L., Borgani S., Dolag K., Matteucci F., 2007, MNRAS, 382, 1050
- Torri E., Meneghetti M., Bartelmann M., Moscardini L., Rasia E., Tormen G., 2004, MNRAS, 349, 476
- Tozzi P., et al., 2015, ApJ, 799, 93
- Vikhlinin A., 2006, ApJ, 640, 710
- Vikhlinin A., et al., 2009, ApJ, 692, 1033
- Voit G.M., 2005, Reviews of Modern Physics, 77, 207
- von der Linden A., et al., 2014, MNRAS, 443, 1973
- Wiersma R.P.C., Schaye J., Theuns T., Dalla Vecchia C., Tornatore L., 2009, MNRAS, 399, 574
- Yoshida N., Sheth R.K., Diaferio A., 2001, MNRAS, 328, 669

APPENDIX A: DECOMPOSITION OF THE SLOPES OF COMPOSITED SIGNALS

In this section we derive the features of $M - Y_X$, $L - T_{sl}$, and $L - M$ based on the two fundamental relations: $M - M_g$ and $M - T_{sl}$:

$$M \propto E(z)^{\gamma_{M_g}} \times M_g^{\beta_{M_g}} \rightarrow M_g \propto E(z)^{-\frac{\gamma_{M_g}}{\beta_{M_g}}} \times M^{\frac{1}{\beta_{M_g}}} \quad (\text{A1})$$

$$M \propto E(z)^{\gamma_{T_{sl}}} \times T_{sl}^{\beta_{T_{sl}}} \rightarrow T_{sl} \propto E(z)^{-\frac{\gamma_{T_{sl}}}{\beta_{T_{sl}}}} \times M^{\frac{1}{\beta_{T_{sl}}}}. \quad (\text{A2})$$

The $M - Y_X$ relation. By definition the Y_X is the product of gas mass and temperature, and thus

$$Y_X = M_g \times T_{sl} \propto E(z)^{-\gamma_{M_g} - \gamma_{T_{sl}}} \times M^{-\beta_{M_g}}. \quad (\text{A3})$$

From eqns. (1)-(3), one deduces

$$Y_X \propto M^{\frac{1}{\beta_{M_g}}} \times E(z)^{-\frac{\gamma_{M_g}}{\beta_{M_g}}} \times M^{\frac{1}{\beta_{T_{sl}}}} \times E(z)^{-\frac{\gamma_{T_{sl}}}{\beta_{T_{sl}}}}. \quad (\text{A4})$$

Writing $M - Y_X$ in general form

$$M = C_{Y_X} \times E(z)^{\gamma_{Y_X}} \times \left(\frac{Y_X}{Y_{X0}} \right)^{\beta_{Y_X}}, \quad (\text{A5})$$

the slope and power of evolution of the $M - Y$ are given by

$$\beta_{Y_X} = \frac{1}{1/\beta_{M_g} + 1/\beta_{T_{sl}}}, \quad (\text{A6})$$

$$\gamma_{Y_X} = \frac{\gamma_{M_g}/\beta_{M_g} + \gamma_{T_{sl}}/\beta_{T_{sl}}}{1/\beta_{M_g} + 1/\beta_{T_{sl}}}. \quad (\text{A7})$$

The $L - T_{sl}$ relation. The general form of $L - T_{sl}$ is given by

$$L = C_{LT} \times E(z)^{\gamma_{LT}} \times \left(\frac{T_{sl}}{T_0} \right)^{\beta_{LT}}. \quad (\text{A8})$$

Recalling that L is related to the total mass and temperature via eqn. 8

$$\begin{aligned} L &\propto E(z)^2 f_g^2 \times M \times T_{sl}^{1/2} \\ &\propto E(z)^2 \times \frac{M_g^2}{M} \times T_{sl}^{1/2} \\ &\propto E(z)^2 \times E(z)^{-\frac{2\gamma_{M_g}}{\beta_{M_g}}} \times M^{\frac{2}{\beta_{M_g}} - 1} \times T_{sl}^{1/2}. \end{aligned} \quad (\text{A9})$$

In the last derivation we use eqn. (1) to rewrite M_g in term of M . In turn, by substituting M in term of T_{sl} via eqn. (2) one obtains

$$\begin{aligned} L &\propto E(z)^2 \times E(z)^{-\frac{2\gamma_{M_g}}{\beta_{M_g}}} \times E(z)^{\gamma_{T_{sl}} \times (\frac{2}{\beta_{M_g}} - 1)} \times T_{sl}^{\beta_{T_{sl}} (\frac{2}{\beta_{M_g}} - 1)} \\ &\propto E(z)^{2(1 - \frac{\gamma_{M_g}}{\beta_{M_g}}) + \gamma_{T_{sl}} (\frac{2}{\beta_{M_g}} - 1)} \times T_{sl}^{\beta_{T_{sl}} (\frac{2}{\beta_{M_g}} - 1) + \frac{1}{2}}. \end{aligned} \quad (\text{A10})$$

By comparing eqn. (10) to eqn. (8) one deduces

$$\beta_{LT} = \beta_{T_{sl}} \left(\frac{2}{\beta_{M_g}} - 1 \right) + \frac{1}{2}, \quad (\text{A11})$$

$$\gamma_{LT} = 2 \left(1 - \frac{\gamma_{M_g}}{\beta_{M_g}} \right) + \gamma_{T_{sl}} \left(\frac{2}{\beta_{M_g}} - 1 \right). \quad (\text{A12})$$

The $L - M$ relation. We define the general form of $L - M$ as

$$L = C_{LM} \times E(z)^{\gamma_{LM}} \times \left(\frac{M}{M_0} \right)^{\beta_{LM}}. \quad (\text{A13})$$

In eqn. (9), we rewrite T_{sl} in term of M via eqn. (2) and obtain

$$\begin{aligned} L &\propto E(z)^2 \times E(z)^{-\frac{2\gamma_{M_g}}{\beta_{M_g}}} \times M^{\frac{2}{\beta_{M_g}} - 1} \times E(z)^{-\frac{\gamma_{T_{sl}}}{2\beta_{T_{sl}}}} \times M^{\frac{1}{2\beta_{T_{sl}}}} \\ L &\propto E(z)^{2(1 - \frac{\gamma_{M_g}}{\beta_{M_g}}) - \frac{\gamma_{T_{sl}}}{2\beta_{T_{sl}}}} \times M^{\frac{2}{\beta_{M_g}} + \frac{1}{2\beta_{T_{sl}}} - 1}. \end{aligned} \quad (\text{A14})$$

From the last equation we can derive the slope and evolution of the LM relation given as

$$\beta_{LM} = \frac{2}{\beta_{M_g}} + \frac{1}{2\beta_{T_{sl}}} - 1, \quad (\text{A15})$$

$$\gamma_{LM} = 2 \left(1 - \frac{\gamma_{M_g}}{\beta_{M_g}} \right) - \frac{1}{2} \frac{\gamma_{T_{sl}}}{\beta_{T_{sl}}}. \quad (\text{A16})$$